Journal of Sound and Vibration 325 (2009) 552–564

Contents lists available at ScienceDirect

Journal of Sound and Vibration

journal homepage: www.elsevier.com/locate/jsvi

Wave pattern motion and stick–slip limit cycle oscillation of a disc brake

Jaeyoung Kang [a,b,*], Charles M. Krousgrill [a], Farshid Sadeghi [a]

[a] School of Mechanical Engineering, 585 Purdue Mall, Purdue University, West Lafayette, IN 47907-2088, USA
[b] Division of Mechanical and Automotive Engineering, College of Engineering, Kongju National University, Cheonan-Si, Republic of Korea

ARTICLE INFO

Article history:
Received 16 August 2008
Received in revised form
20 March 2009
Accepted 24 March 2009
Handling Editor: C.L. Morfey
Available online 25 April 2009

ABSTRACT

This paper examines the dynamic response of a rotating squealing disc brake subject to distributed nonlinear contact stresses where two brake pads are assumed to be stationary and rigid. The friction stresses produce high-frequency vibrations that exhibit standing or traveling waves on the disc surface. The wave pattern resulting from the binary flutter mechanism of one transverse doublet mode pair is studied here. The results show that the wave pattern is associated with mode-coupling character. For a steady-squealing mode, the stick zone of the contact area is determined by a smooth friction–velocity curve having both negative and positive slopes.

1. Introduction

Disc brake squeal has been the subject of significant research over the past few decades as reviewed by Kinkaid et al. [1] and Ouyang et al. [2]. Generally, the dynamic stability of steady sliding in a brake system is analyzed using the linearized equations of motion. The work by Ouyang et al. [3–5] used a rotating contact load on a stationary disc and investigated the equilibrium instability with respect to system parameters. In more realistic theoretical linear model, a disc brake system can be modeled as a rotating annular plate subject to distributed friction stresses due to contact with two stationary pads. The distributed loading generates non-conservative work that can lead to flutter instability [6–10]. This flutter instability is attributed to friction-coupling among certain modes of the system. One of the typical unstable friction-coupling modes is the transverse doublet mode pair. The doublet mode pair has been found to generate the binary flutter instability under critical conditions associated with frequency separation, contact stiffness, contact span angle and other factors [8].

When the flutter instability of the disc arises, the amplitude of vibration response increases, resulting in the need for nonlinear equations of motion to describe the vibration response. Hu et al. [11] demonstrated time histories of rotor vibration and the associated squeal frequencies using nonlinear, transient finite element analysis. Their model considered nonlinear contact kinematics, but neglected disc rotation and radial friction force that have been recently proposed by Hochlenert et al. [12]. As a result, the dissipative mechanism due to the decrease of disc rotating speed was not addressed.

One major portion of the experimental studies on brake squeal has been the wave pattern motion of a squealing disc brake assembly [1]. Holographic techniques such as DPHI (double pulsed holographic interferometry, Fieldhouse et al. [13] and Talbot et al. [14]) and ESPI (high-speed electronic speckle pattern interferometry, Reeves et al. [15] and Krupka et al. [16]) have been used to visualize the vibration pattern on the surface of a squealing disc. The series of time-consecutive

* Corresponding author at: Division of Mechanical and Automotive Engineering, College of Engineering, Kongju National University, Cheonan-Si, Republic of Korea.
E-mail addresses: jkang@kongju.ac.kr (J. Kang), krousgri@ecn.purdue.edu (C.M. Krousgrill), sadeghi@ecn.purdue.edu (F. Sadeghi).

0022-460X/$ - see front matter © 2009 Elsevier Ltd. All rights reserved.
doi:10.1016/j.jsv.2009.03.030

images of the squealing disc provide the vibration pattern of the "n"th mode (n is the nodal diameter) and its mobility (either traveling or standing). Reeves et al. [15] proposed a combination of a pair of modal waveforms to express the experimentally observed wave patterns. Talbot et al. [14] considered fitting the experimental nodal lines as a superposition of multiple waveforms in the Fourier series. Fitting the experimental data to mathematical waveforms provides the clue that the dynamic solution of a nonlinear squealing disc can be approximately expressed in the modal expansion form. Recently, Giannini et al. [17] have reported on the observation of a pure traveling wave of a squealing disc brake using a vibrometer laser scan. They proposed that the traveling wave was generated from the two stationary waves with the same amplitude and a 90° phase difference.

The literature on spinning discs interprets a single vibration mode as the superposition of two (forward and backward) traveling waves [18]. The resonant condition is possible when the disc rotation speed matches the critical rotation speed [19]. In application to automotive brake systems, however, the disc speed never reaches the critical speed associated with a high-frequency squeal mode. Alternately, Flint et al. [7] demonstrated that the deflection shape of a flexible beam travels forward by the numerical solutions obtained from the linearized equations of motion. Unfortunately, there is as yet no analytical approach explaining the experimental wave pattern behavior of a squealing disc brake.

In the current paper, a disc brake model with nonlinear, distributed contact stresses over the contact area is developed. The normal and friction stresses are described on the rotating deformable surface of the disc. The solution of the out-of-plane vibration in an axi-symmetric disc with nonlinear contact kinematics can be expressed as a Fourier series in the circumferential coordinate (θ) with the radial spatial distribution of the response being approximated by the linear vibration modes of the disc. Throughout the numerical time and area integrations, the binary flutter mechanism is shown to generate a traveling wave pattern depending on the mode-coupling character.

2. Nonlinear equations of motion with linearized contact model

The nonlinear dynamic response of disc brake system subject to distributed friction stresses on a deformable contact surface (Fig. 1a) is to be investigated. The contact area is modeled as an annular sector shape with the inner and outer radii r_i and r_o, respectively, and the contact span angle (θ_c) as shown in Fig. 1b. The disc is subject to clamped boundary condition in all directions at the inner radius (a_i) of the rotating shaft with a constant rotating speed (Ω) and a free boundary condition at the outer radius (a_o). A pre-stress $p_o(= N_o/A_c)$ is uniformly applied over the contact area on both sides of the rotating disc, where N_o and A_c are the pre-normal load and contact area, respectively.

The contact kinematics between the rotating disc and the stationary friction material are described on the deformed surface of the disc as shown in Fig. 2. The transverse displacement is denoted as $\tilde{w}$ in the local coordinates (r, φ) attached to the rotating disc and w in the reference coordinates (r, θ) of the global frame. The unit vector $\mathbf{n_a}$ is normal to the top surface of the deformed disc. Friction material is assumed to have no in-plane deformation in such a manner that the contact point b' is in contact with a' of the disc at current time t and the in-plane motion of b' is neglected. Hence, the displacement at b' follows:

$$\langle \mathbf{u_{b'}}, \mathbf{e_z} \rangle = \langle \mathbf{u_{a'}}, \mathbf{e_z} \rangle, \quad \langle \mathbf{u_{b'}}, \mathbf{e_r} \rangle = 0 \quad \text{and } \langle \mathbf{u_{b'}}, \mathbf{e_\theta} \rangle = 0, \tag{1}$$

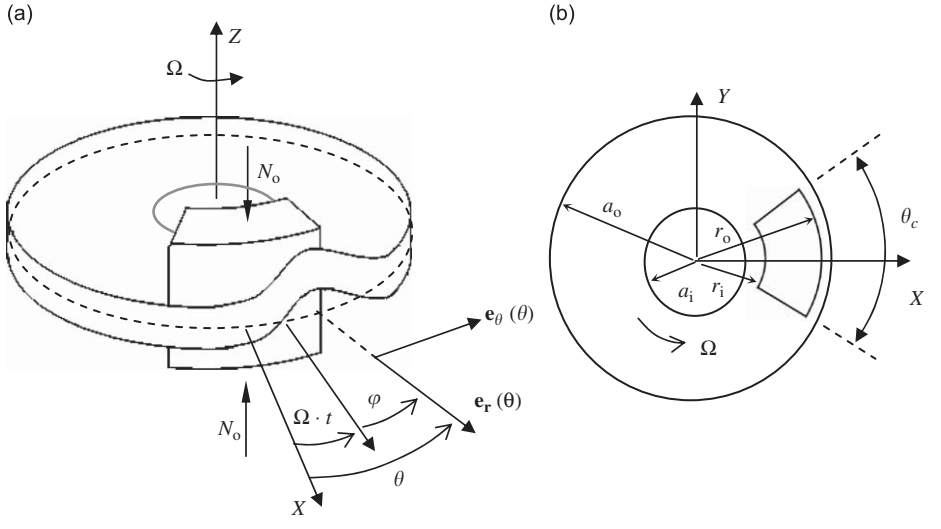

Fig. 1. Rotating deformable disc configuration with two contact interfaces: (a) reference coordinates (r, θ) and local coordinates (r, φ) and (b) disc and contact geometry.

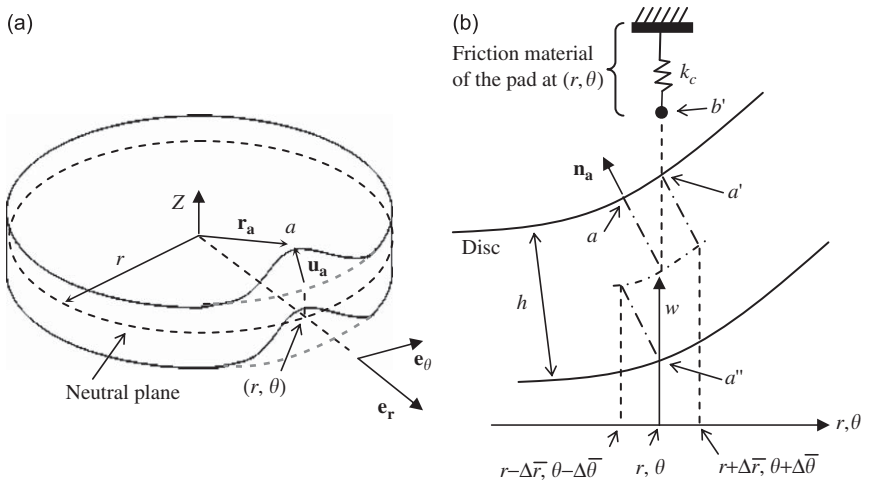

Fig. 2. Description of contact point: (a) position and displacement vectors, $\mathbf{r_a}$ and $\mathbf{u_a}$ of the perturbed contact position, a at (r,θ) in current configuration and (b) contact positions, a' and b′ in 2D figure.

where $\langle\cdot,\cdot\rangle$ denotes the inner product. Also, the displacement vector at the perturbed position a of the disc can be described under the assumption that the in-plane components of the displacement vary linearly through the thickness due to the small oscillation of a squealing thin disc:

$$\mathbf{u_a} = \mathbf{r_a} - \left(r\cdot\mathbf{e_r} + \frac{h}{2}\mathbf{e_z}\right), \tag{2}$$

where

$$\mathbf{r_a} = r\cdot\mathbf{e_r} + \tilde{w}(r,\varphi,t)\mathbf{e_z} + \frac{h}{2}\mathbf{n_a}, \tag{3}$$

$$\mathbf{n_a} = \frac{\nabla\mathbf{f_a}}{|\nabla\mathbf{f_a}|}, \tag{4}$$

$$\nabla\mathbf{f_a} = \mathbf{e_z} - \frac{\partial w}{\partial r}\mathbf{e_r} - \frac{\partial w}{r\partial\theta}\mathbf{e_\theta}. \tag{5}$$

The corresponding velocity vector is obtained by the time-derivative in the reference coordinates:

$$\mathbf{V_a} = \frac{D\mathbf{r_a}}{Dt}, \tag{6}$$

where the coordinate transformation from the local to reference coordinates is given by

$$\frac{D\tilde{w}(r,\varphi,t)}{Dt} = \frac{\partial w(r,\theta,t)}{\partial t} + \Omega\cdot\frac{\partial w(r,\theta,t)}{\partial\theta}. \tag{7}$$

The normal vector ($\mathbf{n_{a'}}$), displacement ($\mathbf{u_{a'}}$) and velocity ($\mathbf{V_{a'}}$) at a' of the deformable disc (Fig. 2b) are obtained by a Taylor series expansion on Eqs. (2)–(6):

$$\mathbf{n_{a'}} = \frac{\nabla\mathbf{f_{a'}}}{|\nabla\mathbf{f_{a'}}|}, \tag{8}$$

$$\mathbf{u_{a'}} = \mathbf{u_a} + \frac{\partial\mathbf{u_a}}{\partial r}\Delta\bar{r} + \frac{\partial\mathbf{u_a}}{\partial\theta}\Delta\bar{\theta} + \text{h.o.t.}, \tag{9}$$

$$\mathbf{V_{a'}} = \mathbf{V_a} + \frac{\partial\mathbf{V_a}}{\partial r}\Delta\bar{r} + \frac{\partial\mathbf{V_a}}{\partial\theta}\Delta\bar{\theta} + \text{h.o.t.}, \tag{10}$$

where

$$\nabla\mathbf{f_{a'}} = \nabla\mathbf{f_a} + \frac{\partial\nabla\mathbf{f_a}}{\partial r}\Delta\bar{r} + \frac{\partial\nabla\mathbf{f_a}}{\partial\theta}\Delta\bar{\theta} + \text{h.o.t.}, \tag{11}$$

$$\Delta\bar{r} = \frac{h}{2}\frac{\partial w(r,\theta,t)}{\partial r} + \text{h.o.t.}, \tag{12}$$

$$r\Delta\bar{\theta} = \frac{h}{2}\frac{\partial w(r,\theta,t)}{r\partial\theta} + \text{h.o.t.}. \tag{13}$$

In the linearized contact models [10,12] above, the higher order terms (h.o.t.) are neglected under the assumption that the squealing oscillations are small.

Coulomb friction is enforced at a' between the disc and a stationary spring element as shown in Fig. 3 to produce:

$$\mathbf{F} = -(\mu \times N)\mathbf{d}, \tag{14}$$

$$\mathbf{N} = -N \times \mathbf{n}_{\mathbf{a}'}, \tag{15}$$

where

$$\mathbf{d} = \frac{\mathbf{V}_{\mathbf{a}'} - \mathbf{V}_{\mathbf{b}'}}{|\mathbf{V}_{\mathbf{a}'} - \mathbf{V}_{\mathbf{b}'}|}, \tag{16}$$

$$\mathbf{V}_{\mathbf{b}'} = \left\langle \frac{\partial \mathbf{u}_{\mathbf{a}'}}{\partial t}, \mathbf{e}_{\mathbf{z}} \right\rangle \mathbf{e}_{\mathbf{z}}. \tag{17}$$

The force balance on a single contact spring element in the Z-direction provides the nonlinear relationship such that

$$N = \frac{p_o + k_c\langle \mathbf{u}_{\mathbf{a}'}, \mathbf{e}_{\mathbf{z}}\rangle}{\langle(\mu \times \mathbf{d} + \mathbf{n}_{\mathbf{a}'}), \mathbf{e}_{\mathbf{z}}\rangle}. \tag{18}$$

Here, the friction coefficient μ on the top of the disc is expressed as a smooth friction curve [20]:

$$\mu(r,t) = |(1 - e^{-\beta_2|\mathbf{V}_{\mathbf{slip}}|}) \times \{\mu_k + (\mu_s - \mu_k)e^{-\beta_1|\mathbf{V}_{\mathbf{slip}}|}\}|, \tag{19}$$

where μ_s, μ_k, β_1 and β_2 are the control parameters determining the magnitude and slope of the friction coefficient and $\mathbf{V}_{\mathbf{slip}} = \mathbf{V}_{\mathbf{a}'} - \mathbf{V}_{\mathbf{b}'}$.

The discretized equations of motion for the friction-coupled disc system are derived in terms of modal coordinates, $\{q_n\}_{n=1,2,\ldots,N_d}$ through the assumed modes method:

$$\frac{\mathrm{d}}{\mathrm{d}t}\left[\frac{\partial L}{\partial \dot{q}_m}\right] - \frac{\partial L}{\partial q_m} = \sum_{n=1}^{N_d} Q_{mn}(q_n), \quad m = 1,\ldots,N_d, \tag{20}$$

$$L = T - (U + U_c), \tag{21}$$

where U is the strain energy of the component disc and

$$T = \frac{\rho h}{2} \times \int_0^{2\pi}\int_{a_i}^{a_o}\left[\frac{\partial w(r,\theta,t)}{\partial t} + \Omega\frac{\partial w(r,\theta,t)}{\partial\theta}\right]^2 r\,\mathrm{d}r\,\mathrm{d}\theta, \tag{22}$$

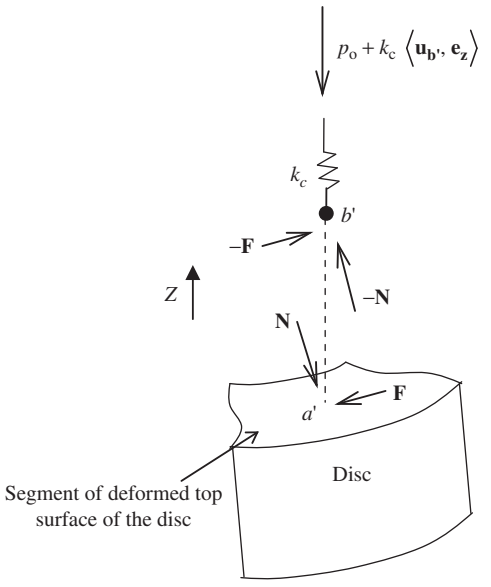

Fig. 3. Contact stresses at a' and b' in current configuration, k_c is contact stiffness.

$$U_c = U_{c,\text{top}} + U_{c,\text{bottom}}, \tag{23}$$

$$\delta W \equiv \sum_{m=1}^{N_d}\sum_{n=1}^{N_d} Q_{mn}(q_n)\cdot\delta q_m = \delta W_{\text{top}} + \delta W_{\text{bottom}}. \tag{24}$$

Here the virtual work (δW) done by the contact stresses and the contact strain energy (U_c) due to contact stiffness over the top contact area are expressed as

$$\delta W_{\text{top}} = \int_{-\theta_c/2}^{\theta_c/2}\int_{r_i}^{r_o}\{\langle(\mathbf{N}+\mathbf{F}),\delta\mathbf{u}_{\mathbf{a}'}\rangle - \langle(\mathbf{N}+\mathbf{F}),\delta\mathbf{u}_{\mathbf{b}'}\rangle\}r\,\mathrm{d}r\,\mathrm{d}\theta, \tag{25}$$

$$U_{c,\text{top}} = \frac{k_c}{2}\int_{-\theta_c/2}^{\theta_c/2}\int_{r_i}^{r_o}\langle\mathbf{u}_{\mathbf{b}'},\mathbf{e}_{\mathbf{z}}\rangle^2 r\,\mathrm{d}r\,\mathrm{d}\theta. \tag{26}$$

The virtual work and contact strain energy on the bottom contact, δW_{bottom} and $U_{c,\text{bottom}}$ are similarly obtained by

$$\delta W_{\text{bottom}} = \int_{-\theta_c/2}^{\theta_c/2}\int_{r_i}^{r_o}\{\langle(\mathbf{N}'+\mathbf{F}'),\delta\mathbf{u}_{\mathbf{a}''}\rangle - \langle(\mathbf{N}'+\mathbf{F}'),\delta\mathbf{u}_{\mathbf{b}''}\rangle\}r\,\mathrm{d}r\,\mathrm{d}\theta, \tag{27}$$

$$U_{c,\text{bottom}} = \frac{k_c}{2}\int_{-\theta_c/2}^{\theta_c/2}\int_{r_i}^{r_o}\langle\mathbf{u}_{\mathbf{b}''},\mathbf{e}_{\mathbf{z}}\rangle^2 r\,\mathrm{d}r\,\mathrm{d}\theta, \tag{28}$$

where $\mathbf{N}'$ and $\mathbf{F}'$ denote the normal and friction force acting at a'' and where b'' denotes the contact position of the bottom friction material in contact with a''.

The trial functions used in the above assumed modes model will be the linear vibration modes of the stationary disc:

$$w(r,\theta,t) \cong \sum_{n=1}^{N_d/2} R_n(r)\{\cos n\theta\times q_{2n-1}(t) + \sin n\theta\times q_{2n}(t)\}, \tag{29}$$

where $\{R_n(r)\}_{n=1,\ldots,N_d/2}$ is the radial eigenfunction with the nth nodal diameter obtained from Bessel functions [8] satisfying the prescribed boundary conditions. For mass-normalization, the radial function is set to be $\rho h\pi\int_{a_i}^{a_o} R_n^2 r\,\mathrm{d}r \equiv 1$. The subsequent numerical eigenfunctions of the disc are calculated for density ($7150\,\mathrm{kg\,m^{-3}}$), Young's modulus (88.9 GPa) and Poisson's ratio (0.285).

A single doublet mode pair model of the disc has been shown to be effective in predicting the flutter instability of squeal by Kang et al. [8]. The binary mode approximation can provide the essential character of the squealing disc. Therefore, the squeal mode of the squealing disc is expressed in the form of the nth doublet mode pair:

$$w(r,\theta,t) = R_n(r)\{\cos(n\theta)\times a_1(t) + \sin(n\theta)\times a_2(t)\}, \tag{30}$$

where the modal coordinates a_1 and a_2 are to be determined. Substitution of Eq. (30) into Eq. (20) produces the nonlinear equations of motion for the one doublet-mode pair. In the next section, the theory for wave pattern motion associated with the one-doublet binary mode is proposed and the numerical results for the system parameters in Table 1 are illustrated.

3. Wave pattern: standing wave and traveling wave

The wave pattern motion of disc brake system has been observed experimentally using holographic techniques [13–16]. However, this work does not explain why a surface of the squealing disc brake exhibits either a standing wave or a traveling wave and what determines the wave pattern of the disc surface during squeal. The analytical approach may provide the mechanism determining the wave pattern motion. A single doublet mode pair model is used in the following manner.

The wave pattern motion for a single doublet mode pair can be determined from the so-called wave pattern index $\psi(t)$:

$$\psi(t) = \dot{a}_2(t)\times a_1(t) - a_2(t)\times\dot{a}_1(t). \tag{31}$$

In Appendix A, it is shown that

$$\psi(t) > 0: \text{ forward traveling wave (FWD)}, \tag{32}$$

Table 1
Nominal values of system parameters.

a_o (mm)	a_i (mm)	h (mm)	r_o (mm)	r_i (mm)	θ_c (°)	k_c ($\mathrm{N\,m^{-3}}$)	N_o (N)
150	90	13	142	100	62	0.35×10^{11}	2000

$$\psi(t)<0: \text{ backward traveling wave (BWD)}, \tag{33}$$

$$\psi(t)=0 \quad \text{and} \quad \frac{\mathrm{d}\psi(t)}{\mathrm{d}t}\neq 0: \text{ instantaneous standing (IS) wave}, \tag{34}$$

$$\psi(t)=0 \quad \text{and} \quad \frac{\mathrm{d}\psi(t)}{\mathrm{d}t}=0 \text{ (for sufficient time)}: \text{ standing wave}. \tag{35}$$

Through linearization of the nonlinear equations of motion (20) about a steady-sliding state, the analytical solutions for the wave pattern motion can be obtained. It is notable that nonlinearity obtaining from contact kinematics of Eq. (16) and (18) and friction curve of Eq. (19) has been linearized in this process. The corresponding linearized equations of motion for one doublet mode pair are expressed in the matrix form:

$$\begin{Bmatrix} \ddot{a}_1 \\ \ddot{a}_2 \end{Bmatrix} + \begin{bmatrix} D_1 & 2n\Omega \\ -2n\Omega & D_2 \end{bmatrix} \begin{Bmatrix} \dot{a}_1 \\ \dot{a}_2 \end{Bmatrix} + \begin{bmatrix} \Omega_1^2 & b_1 \\ b_2 & \Omega_1^2 \end{bmatrix} \begin{Bmatrix} a_1 \\ a_2 \end{Bmatrix} = 0, \tag{36}$$

where components of Eq. (36) are described in Appendix B. The mode-coupling instability of one transverse doublet mode pair with constant friction coefficient was already investigated in Ref. [8]. The destabilizing effect of mode-coupling under constant friction coefficient is dominant, whereas the negative friction-slope denoted by N_{s1} and N_{s2}, respectively, of D_1 and D_2 in Eqs. (B.3) and (B.4) makes supplementary effect [10]. Here, D_1 and D_2 represent for the positive damping due to system structural damping and radial dissipative effect and the negative damping obtained from the negative friction-slope. The off-diagonal elements, b_1 and b_2 of the stiffness matrix stem from the friction-coupling between the doublet mode pair. Their closed-form solutions are sought for the case when the modal damping coefficients are identical ($D_1 = D_2 \equiv D$) in the absence of gyroscopic effects. The numerical solutions for the general case will be provided later. For the non-gyroscopic case with identical damping coefficients, the eigenvalues λ and eigenvectors $\mathbf{V}$ corresponding to Eq. (36) are

$$\lambda_{1,2} = -\frac{D}{2} \pm \frac{1}{2}\sqrt{D^2 - 2(\Omega_1^2+\Omega_2^2) + 2\sqrt{(\Omega_1^2+\Omega_2^2)^2 + 4b_1b_2}}, \tag{37}$$

$$\lambda_{3,4} = -\frac{D}{2} \pm \frac{1}{2}\sqrt{D^2 - 2(\Omega_1^2+\Omega_2^2) - 2\sqrt{(\Omega_1^2+\Omega_2^2)^2 + 4b_1b_2}}, \tag{38}$$

$$\mathbf{V_{1,2}} = \begin{Bmatrix} \frac{1}{2b_2}\left[(\Omega_1^2-\Omega_2^2) - \sqrt{(\Omega_1^2-\Omega_2^2)^2+4b_1b_2}\right] \\ 1 \end{Bmatrix}, \tag{39}$$

$$\mathbf{V_{3,4}} = \begin{Bmatrix} \frac{1}{2b_2}\left[(\Omega_1^2-\Omega_2^2) + \sqrt{(\Omega_1^2-\Omega_2^2)^2+4b_1b_2}\right] \\ 1 \end{Bmatrix}, \tag{40}$$

where the zero frequency case ($\mathrm{Im}(\lambda)=0$) in the following analysis is excluded due to the nature of squeal vibrations.

For non-merged binary modes; $(\Omega_1^2-\Omega_2^2)^2 + 4b_1b_2 > 0$, the eigenvalues and eigenvectors can be expressed as

$$\lambda_{1,2} \equiv -\frac{D}{2} \pm \mathrm{i}\Lambda_1 \quad \text{and} \quad \lambda_{3,4} \equiv -\frac{D}{2} \pm \mathrm{i}\Lambda_2, \tag{41}$$

$$\mathbf{V_{1,2}} \equiv \begin{Bmatrix} u_1 \\ 1 \end{Bmatrix} \quad \text{and} \quad \mathbf{V_{3,4}} \equiv \begin{Bmatrix} u_2 \\ 1 \end{Bmatrix}, \tag{42}$$

where Λ_1 and Λ_2 ($\neq\Lambda_1$) are the modal circular frequencies and u_1 and $u_2(\neq u_1)$are real. For mode-merged binary modes; $(\Omega_1^2-\Omega_2^2)^2 + 4b_1b_2 < 0$, the eigensolutions are

$$\lambda_{1,2} \equiv -\frac{D}{2} \pm (\alpha + \mathrm{i}\omega) \quad \text{and} \quad \lambda_{3,4} \equiv -\frac{D}{2} \pm (\alpha - \mathrm{i}\omega), \tag{43}$$

$$\mathbf{V_{1,2}} \equiv \begin{Bmatrix} u \\ 1 \end{Bmatrix} - \mathrm{i}\begin{Bmatrix} v \\ 0 \end{Bmatrix} \quad \text{and} \quad \mathbf{V_{3,4}} \equiv \begin{Bmatrix} u \\ 1 \end{Bmatrix} + \mathrm{i}\begin{Bmatrix} v \\ 0 \end{Bmatrix}, \tag{44}$$

where ω is the merged circular frequency and $\alpha(>0)$, $v(<0)$ and u are real. From the abbreviated form of eigensolutions, the general solutions $w_A(r,\theta,t)$ and $w_B(r,\theta,t)$ of Eq. (30), respectively, for non-merged modes and mode-merged binary modes can be rewritten as the linear combination of eigenvectors (42) and (44) such that

$$\begin{aligned} w_A(r,\theta,t) = {} & \mathrm{e}^{t(-D/2)} R_n[\cos(n\cdot\theta)\{A_1 \times u_1 \cos(\Lambda_1\cdot t) + A_2 \times u_2 \cos(\Lambda_2\cdot t)\} \\ & + \sin(n\cdot\theta)\{A_1 \cos(\Lambda_1\cdot t) + A_2 \cos(\Lambda_2\cdot t)\}, \end{aligned} \tag{45}$$

$$\begin{aligned} w_B(r,\theta,t) = {} & e^{t(\alpha-D/2)}R_n[\cos(n\cdot\theta)\{B_1(u\cos(\omega t)+v\sin(\omega t))+B_2(u\sin(\omega t)-v\cos(\omega t))\} \\ & +\sin(n\cdot\theta)\{B_1\cos(\omega t)+B_2\sin(\omega t)\}] \\ & +e^{t(-\alpha-D/2)}R_n[\cos(n\cdot\theta)\{B_3(u\cos(\omega t)-v\sin(\omega t))+B_4(-u\sin(\omega t)-v\cos(\omega t))\} \\ & +\sin(n\cdot\theta)\{B_3\cos(\omega t)-B_4\sin(\omega t)\}], \end{aligned} \tag{46}$$

where the decaying terms associated with $e^{-\alpha t}$ are neglected in Eq. (46) and where (A_1, A_2) and (B_1, B_2, B_3, B_4) depend on initial conditions. In turn, the wave pattern indices, $\psi_A(t)$ and $\psi_B(t)$ are calculated for Eqs. (45) and (46) as

$$\psi_A(t) = \tfrac{1}{2}A_1A_2(u_2-u_1)[(\Lambda_1+\Lambda_2)\sin\{(\Lambda_1-\Lambda_2)t\}+(\Lambda_1-\Lambda_2)\sin\{(\Lambda_1+\Lambda_2)t\}], \tag{47}$$

$$\psi_B(t) = -(B_1^2+B_2^2)v\times\omega>0. \tag{48}$$

Since the squeal frequencies are high with small frequency separation, $|\Lambda_1+\Lambda_2|\gg|\Lambda_1-\Lambda_2|$. With this, $\psi_A(t)$ reduces to the simple harmonic function of

$$\psi_A(t) \approx \tfrac{1}{2}A_1A_2(u_2-u_1)\times(\Lambda_1+\Lambda_2)\sin\{(\Lambda_1-\Lambda_2)t\}. \tag{49}$$

Eqs. (48) and (49) indicate that wave pattern is independent of the damping coefficient D.

It is concluded from Eq. (48) that the mode-merged doublet pair should always retain a forward traveling wave near the steady-sliding equilibrium. In contrast, the wave pattern of the non-merged doublet pair switches between forward and backward traveling waves where the instantaneous standing wave appears at the time of transition (t_s) between two patterns which is periodic:

$$t = t_s = \frac{k\pi}{|\Lambda_1-\Lambda_2|}, \quad k = 1,2,\ldots,\infty. \tag{50}$$

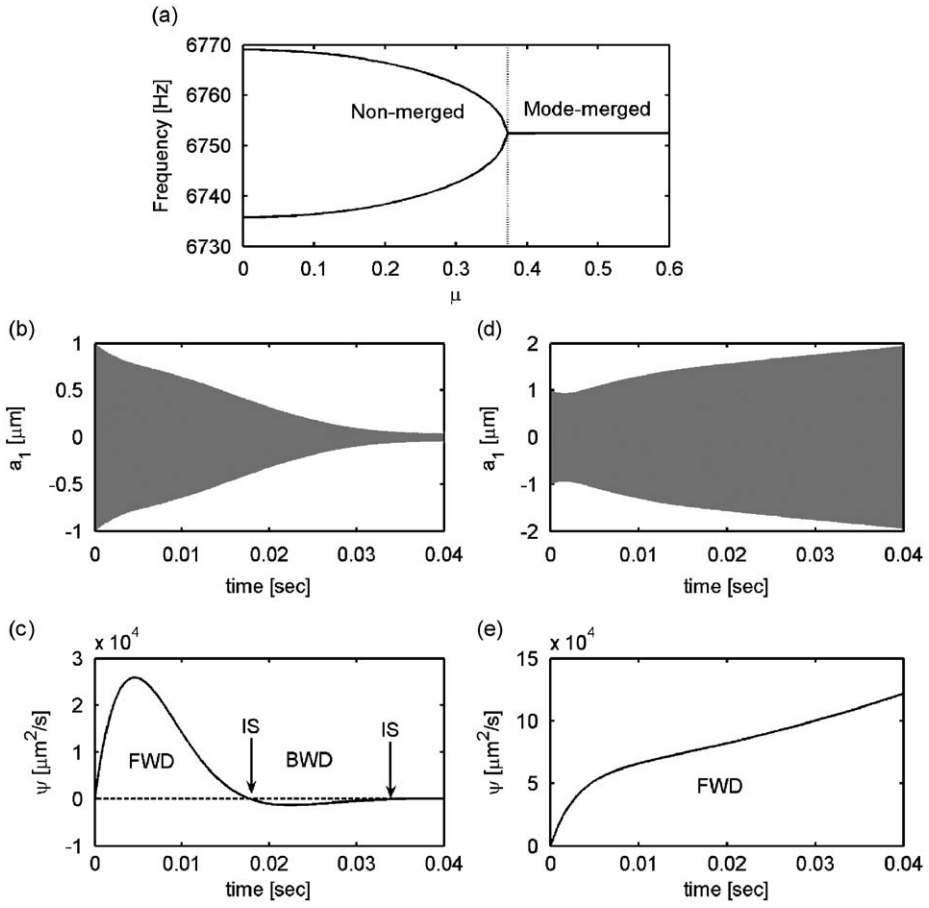

Fig. 4. Wave pattern index for non-merged and merged binary modes ($n=7$): (a) frequency loci, (b) time response at $\mu=0.2$, (c) $\psi(t)$ at $\mu=0.2$, (d) time response at $\mu=0.5$ and (e) $\psi(t)$ at $\mu=0.5$; $D_1=D_2=2\xi_n\omega_n$, $\xi_n=2\times10^{-3}$, $\Omega=0$; FWD, IS and BWD denote the forward traveling, instantaneous standing and backward traveling waves.

From the closed-form solutions of the linearized system, it is found that the wave pattern motion is associated with the mode-coupling of the binary mode pair such as the mode-merged and non-merged states. Fig. 4 illustrates the wave patterns corresponding to the non-merged and mode-merged pair modes, as predicted in Eqs. (48)–(50).

Giannini et al. [17] provided a visualization of an experimentally observed traveling wave pattern of the squealing disc through the capture of out-of-plane mode shapes at six different time frames. In the similar manner, vibration deformation shapes at different frames are numerically calculated here for determining the direction of wave propagation, as illustrated in Fig. 5. It should be highlighted that the wave pattern and the direction of traveling waves in Fig. 5 correspond to the wave pattern index $\psi(t)$ of Fig. 4c.

In the presence of gyroscopic effects and non-identical damping coefficients ($D_1 \neq D_2$), the wave pattern can be determined numerically. Numerical solution of Eq. (36) is obtained using the fourth-order Runge–Kutta method. Fig. 6 exhibits the wave pattern index $\psi(t)$ for the doublet disc pair subject to rotation effects. For the case of $\mu = 0.2$, the duration of backward traveling wave ($\psi(t)<0$) diminishes as the rotation speed increases. In contrast, for $\mu = 0.5$, the wave always travels forward regardless of the rotational speed. In this case, the time response becomes stable for $\Omega = 2\,\mathrm{rad\,s^{-1}}$ due to the increase of damping coefficient associated with radial dissipative effect, but the wave pattern is not changed ($\psi(t)>0$ for all $t>0$).

The wave pattern of a squealing disc subject to nonlinear contact stresses can be also assessed by the numerical solution of Eq. (20). In the subsequent analysis, the friction curve is assumed to have the numerical values: $\mu_s = 0.5$, $\mu_k = 0.3$, $\beta_1 = 20$ and $\beta_2 = 1$. At every time-iteration step of Eqs. (25)–(28), a contact area integration is required. To accomplish this, the contact area is discretized with a grid in both radial and circumferential directions for the numerical area integration in the following manner:

$$\int_{-\theta_c/2}^{\theta_c/2}\int_{r_i}^{r_o}(\ \bullet)r\,\mathrm{d}r\,\mathrm{d}\theta \cong \sum_{i=1}^{M_r}\sum_{j=1}^{M_\theta}(\ \bullet)r_i \times \Delta r_i \times \Delta\theta_j \tag{51}$$

where M_r, M_θ denote the number of the nodes of the contact area, respectively, in the radial and circumferential directions. From convergence studies considering the number of grid points for the integration, a (16×40) grid in the radial and circumferential directions, respectively, is chosen, as shown in Fig. 7.

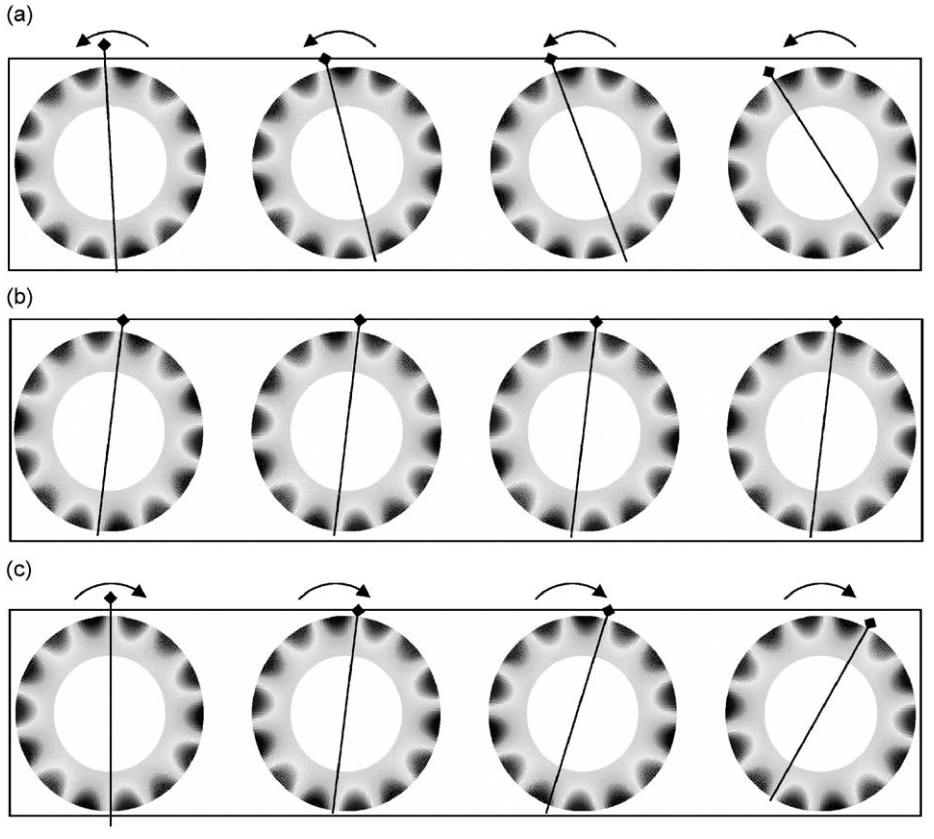

Fig. 5. Mode shapes (4 frames) for non-merged binary modes of Fig. 4c: (a) FWD at $t = 0.008\,\mathrm{s} + k\Delta t$, (b) IS at $t = 0.018\,\mathrm{s} + k\Delta t$ and (c) BWD at $t = 0.024\,\mathrm{s} + k\Delta t$, $\Delta t \approx 1.7 \times 10^{-7}$ s and $k = 1,2,3,4$; friction stresses are defined under the counter-clockwise disc rotation.

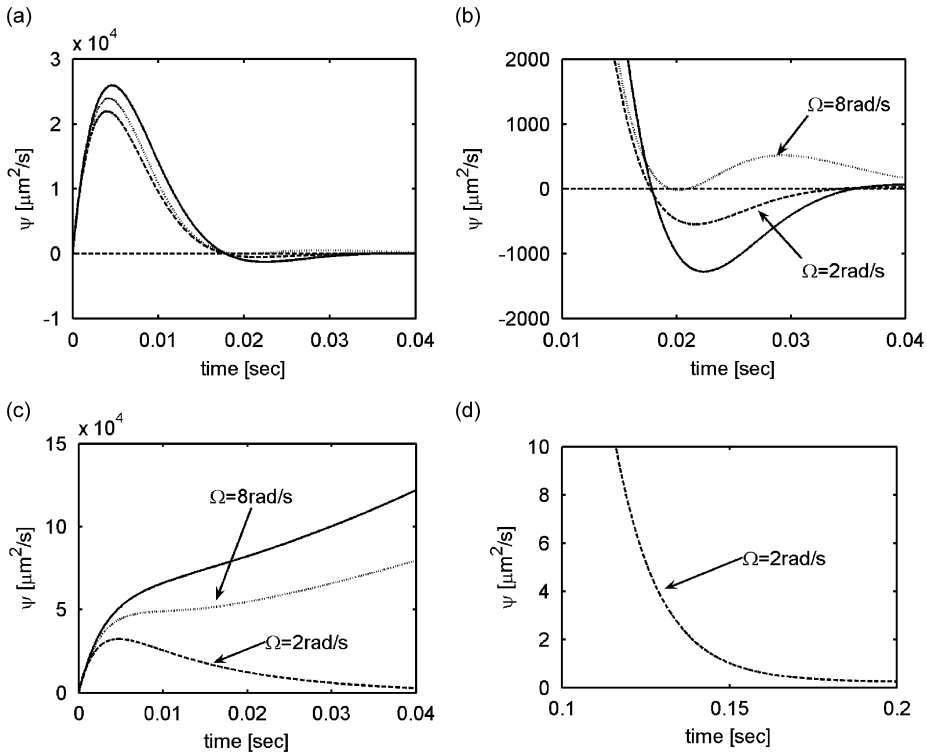

Fig. 6. Rotation effects on wave pattern: (a, b) $\psi(t)$ at $\mu = 0.2$ and (c, d) $\psi(t)$ at $\mu = 0.5$; solid lines are identical to those of Fig. 4.

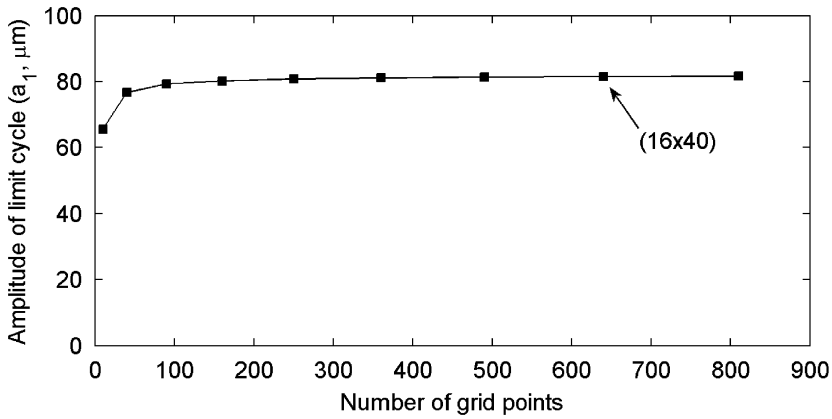

Fig. 7. Convergence check for the numerical area integration with respect to the number of grid points.

Fig. 8a shows an example of limit cycle oscillations resulting from a mode-coupling instability. The corresponding wave pattern of the nonlinear response is found to be a forward traveling wave as illustrated in Fig. 8b. Talbot et al. [14] reported that the out-of-plane vibration and a forward traveling wave around the disc surface were observed in a variety of disc brake systems during squeal. Also, they suggested the possibility of a smaller backward traveling wave, which may be explained by mode-separated binary modes as shown in Figs. 4b and c.

4. Analysis of stick–slip behavior in limit cycle response

In this section, we focus on the stick–slip behavior of a steady-squealing binary mode where the out-of-plane vibration has been found to be a forward traveling waveform. The nonlinear friction curve in Eq. (19) retains two separate sections

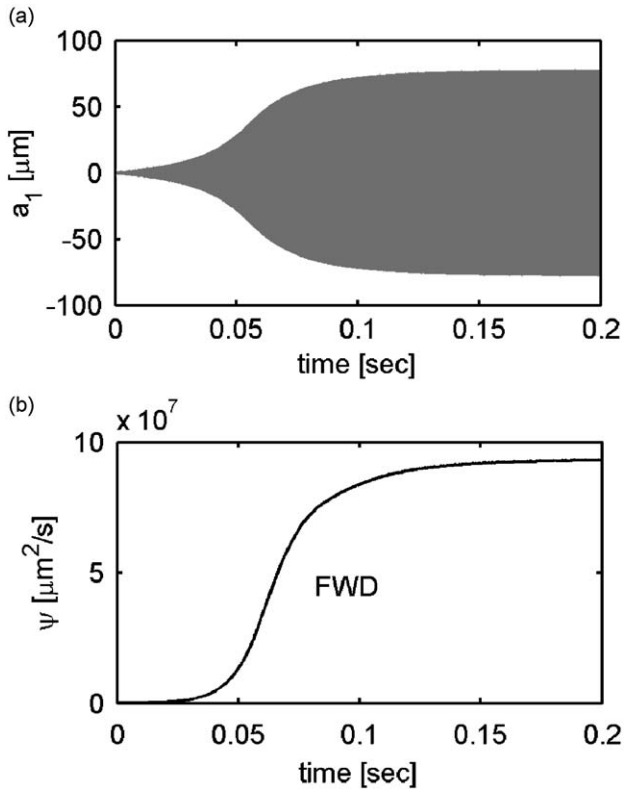

Fig. 8. Limit cycle oscillations and the corresponding wave pattern index for a steady-squealing mode due to binary flutter ($n = 7$) subject to nonlinear contact stresses: (a) $a_1(t)$ and (b) $\psi(t)$, $\Omega = 5\,\mathrm{rad\,s^{-1}}$, $\xi_n = 0.0$.

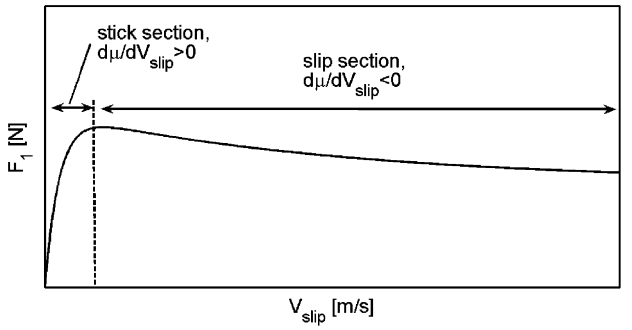

Fig. 9. Determination of stick–slip phase for a qualitatively smooth friction curve: $V_{\mathrm{slip}} = |\mathbf{V}_{\mathbf{a}'} - \mathbf{V}_{\mathbf{b}'}|$.

with respect to the slope of the curve: positive slope, $\mathrm{d}\mu/\mathrm{d}V_{\mathrm{slip}} > 0$ and negative slope, $\mathrm{d}\mu/\mathrm{d}V_{\mathrm{slip}} < 0$. The negative slope of μ becomes one of destabilizing factors (note that mode-coupling due to constant μ is a major destabilizing factor [10]), whereas the positive slope of μ near relative zero velocity can be used to determine the stick phase of stick–slip motion of the steady-squealing mode in the smoothing sense (Fig. 9) [21–23]. In terms of the parameters in friction function of Eq. (19), μ_s, μ_k and β_1 determine negative friction-slope and magnitude of friction coefficient on the basis of experimental data [24]. β_2 describing a creep region is chosen for numerical calculation as a smoothing method which provides a qualitative stick–slip behavior [21–23]. Here, β_2 is meaningful only when the flutter instability associated with (μ_s, μ_k, β_1) occur at the steady-sliding state and the disc oscillation increases up to the point where the relative velocity between the disc rotation speed and vibrational speed approaches zero at certain locations of the contact region. From this, the stick–slip state can be qualitatively determined over the entire contact interface of the disc system during the limit cycle of a squealing mode if the time history of the friction curve is obtained over the area.

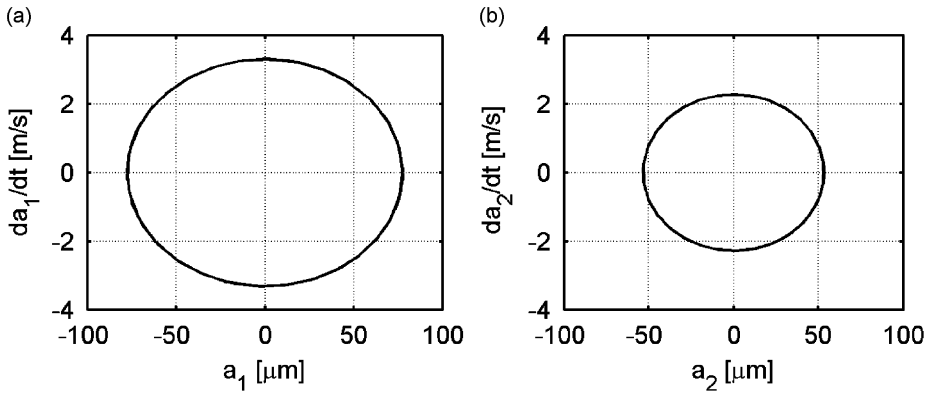

Fig. 10. Response on limit cycle; $\Omega = 5\,\mathrm{rad\,s^{-1}}$, $\xi_n = 0.0$.

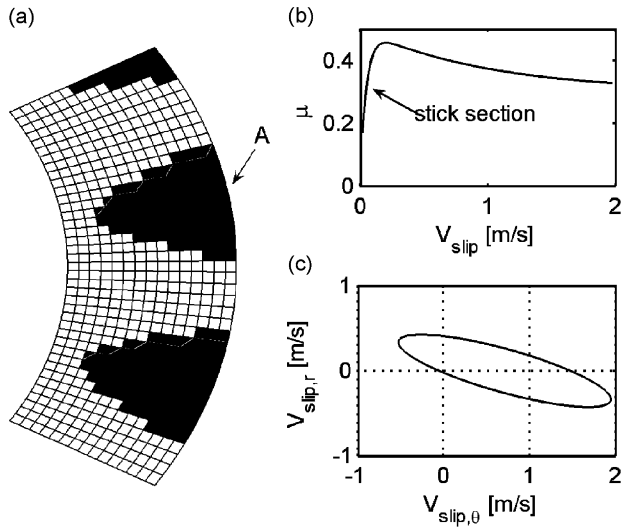

Fig. 11. Stick–slip characteristics on limit cycle of a steady-squealing mode ($n = 7$): (a) stick-zone (shaded) on the contact interface, (b) one cycle of friction curve at "A" and (c) phase plane of slip components at "A"; "A" is located at $(r, \theta) = (r_o, 11^\circ)$; $V_{\mathrm{slip},\theta} \equiv \langle \mathbf{V_{slip}}, \mathbf{e_\theta} \rangle$ and $V_{\mathrm{slip},r} \equiv \langle \mathbf{V_{slip}}, \mathbf{e_r} \rangle$.

Fig. 10 shows the limit cycle of each modal response of the binary flutter modes. For the limit cycle of a steady-squealing binary flutter mode, stick zone is illustrated on the contact area as shown in Fig. 11a, where this zone undergoes stick phase during limit cycle oscillations. A specific location in the stick zone is chosen for the demonstration of stick–slip behavior. The friction coefficient and the components of slip velocity at the selected location are traced over one period as shown in Figs. 11b and c. It is notable that the radial component of slip velocity is not negligible since the radial component makes significant contribution to energy dissipation near zero relative velocity.

5. Conclusions and discussion

The dynamic response of one transverse doublet mode pair of a disc brake due to distributed, nonlinear contact stresses has been investigated under the assumption that two brake pads are stationary and rigid. The analytical solutions of linearized response for the wave pattern motion have been provided near the steady-sliding state of the system. The conclusion for the linear regime is drawn as the following. For a mode-merged binary mode, the squealing waveform of the disc travels forward regardless of disc rotation speed. In contrast, the wave pattern of the mode-separated binary mode switches between a forward and backward traveling wave, where an instantaneous standing wave appears during the transition of two patterns. Also, disc rotation speed is found to influence the wave pattern motion.

The nonlinear response of a squealing disc brake has also been analyzed. For a steady-squealing binary mode, the wave pattern is seen to be a forward traveling wave regardless of the disc rotational speed. The proposed disc brake model also predicts that the dynamic response reaches the limit cycle of the out-of-plane vibration. Throughout the contact area discretization and time-integration, the nonlinear friction coefficient at each finite contact element is calculated and used for the determination of the existence of a stick–phase during one period. It is notable that the stick regime over the contact

area resembles the stationary vibration pattern of a squealing disc. Particularly, the radial component of friction force assumes a significant role on the steady-squealing response.

The nonlinear binary flutter mechanism of a squealing disc allows for a better understanding on the post-onset mechanism. Through linearization of the nonlinear equations of motion, the onset of squeal has been estimated by means of the linear stability analysis. From the nonlinear approach, the theoretical disc brake model can now predict the nonlinear behavior of the squealing disc brake in terms of the squealing frequencies and the corresponding wave pattern motion.

Appendix A. Proof of the wave pattern expression

The binary mode expansion of Eq. (30) can be rewritten as

$$w(r,\theta,t) = [R_n(r) \times \cos\{n\cdot\theta - \phi(t)\}]\{\sqrt{1+\gamma^2(t)} \times a_1(t)\}, \tag{A.1}$$

where $\gamma(t) = a_2(t)/a_1(t)$ and $\phi(t) = \tan^{-1}\{\gamma(t)\}$. If the phase angle increases in time, it represents a forward traveling wave. Alternately, for a decreasing phase angle in time, the wave travels backward. Hence, the direction of the wave propagation for a given time is determined by the rate of change in the phase angle as being a function of the wave pattern index, $\psi(t)$ since

$$\frac{\mathrm{d}\phi(t)}{\mathrm{d}t} = \frac{\dot\gamma(t)}{1+\gamma^2(t)} = \frac{\psi(t)}{\{\dot a_1^2(t) + \dot a_2^2(t)\}}, \tag{A.2}$$

where, again, $\psi(t) = \dot a_2(t)\times a_1(t) - a_2(t)\times \dot a_1(t)$. Therefore, the sign of $\psi(t)$ determines the wave pattern as prescribed in Eqs. (32)–(35).

Appendix B. The elements of the linearized one-doublet mode model

$$R_{d1} = \frac{2p_o}{\Omega}\left(\frac{h}{2}\right)^2 \int_{r_i}^{r_o}\left(\frac{\partial R_n}{\partial r}\right)^2 \mu*(r)\,\mathrm{d}r \times \int_{-\theta_c/2}^{\theta_c/2}\cos^2 n\theta\,\mathrm{d}\theta, \tag{B.1}$$

$$R_{d2} = \frac{2p_o}{\Omega}\left(\frac{h}{2}\right)^2 \int_{r_i}^{r_o}\left(\frac{\partial R_n}{\partial r}\right)^2 \mu*(r)\,\mathrm{d}r \times \int_{-\theta_c/2}^{\theta_c/2}\sin^2 n\theta\,\mathrm{d}\theta, \tag{B.2}$$

$$N_{s1} = 2p_o\left(\frac{nh}{2}\right)^2 \int_{r_i}^{r_o}\left[\frac{R_n^2}{r}\left\{\frac{\partial\mu}{\partial v_{,t}}\bigg|_{\mathbf{f}=\mathbf{0}}\right\}\right]\mathrm{d}r \times \int_{-\theta_c/2}^{\theta_c/2}\sin^2 n\theta\,\mathrm{d}\theta, \tag{B.3}$$

$$N_{s2} = 2p_o\left(\frac{nh}{2}\right)^2 \int_{r_i}^{r_o}\left[\frac{R_n^2}{r}\left\{\frac{\partial\mu}{\partial v_{,t}}\bigg|_{\mathbf{f}=\mathbf{0}}\right\}\right]\mathrm{d}r \times \int_{-\theta_c/2}^{\theta_c/2}\cos^2 n\theta\,\mathrm{d}\theta, \tag{B.4}$$

$$\begin{aligned}\Omega_1^2 = {}& \omega_n^2 - n^2\Omega^2 + 2k_c\int_{r_i}^{r_o} R_n^2(r) r\,\mathrm{d}r \times \int_{-\theta_c/2}^{\theta_c/2}\cos^2 n\theta\,\mathrm{d}\theta \\ & + 2p_o\times n^2\left(\frac{h}{2}\right)\left[\int_{r_i}^{r_o}(1+\mu^*(r)^2)\frac{R_n^2}{r}\,\mathrm{d}r \times \int_{-\theta_c/2}^{\theta_c/2}\sin^2 n\theta\,\mathrm{d}\theta\right] \\ & + 2p_o\times\left(\frac{h}{2}\right)\left[\int_{r_i}^{r_o}\left(\frac{\partial R_n}{\partial r}\right)^2 r\,\mathrm{d}r \times \int_{-\theta_c/2}^{\theta_c/2}\cos^2 n\theta\,\mathrm{d}\theta\right],\end{aligned} \tag{B.5}$$

$$\begin{aligned}\Omega_2^2 = {}& \omega_n^2 - n^2\Omega^2 + 2k_c\int_{r_i}^{r_o} R_n^2(r) r\,\mathrm{d}r \times \int_{-\theta_c/2}^{\theta_c/2}\sin^2 n\theta\,\mathrm{d}\,\theta \\ & + 2p_o\times n^2\left(\frac{h}{2}\right)\left[\int_{r_i}^{r_o}(1+\mu*(r)^2)\frac{R_n^2}{r}\,\mathrm{d}r \times \int_{-\theta_c/2}^{\theta_c/2}\cos^2 n\theta\,\mathrm{d}\,\theta\right] \\ & + 2p_o\times\left(\frac{h}{2}\right)\left[\int_{r_i}^{r_o}\left(\frac{\partial R_n}{\partial r}\right)^2 r\,\mathrm{d}r \times \int_{-\theta_c/2}^{\theta_c/2}\sin^2 n\theta\,\mathrm{d}\,\theta\right]\end{aligned} \tag{B.6}$$

$$b_1 = 2n \times k_c\left(\frac{h}{2}\right)\left\{\int_{r_i}^{r_o} \mu*(r)R_n^2(r)\,\mathrm{d}r \times \int_{-\theta_c/2}^{\theta_c/2} \sin^2 n\theta\,\mathrm{d}\,\theta\right\}$$
$$+ 2p_o \times n^3\left(\frac{h}{2}\right)^2\left[\int_{r_i}^{r_o} \mu*(r)\left(\frac{R_n}{r}\right)^2 \mathrm{d}r \times \int_{-\theta_c/2}^{\theta_c/2} \cos^2 n\theta\,\mathrm{d}\,\theta\right]$$
$$+ 2p_o \times \left(\frac{h}{2}\right)^2\left[\int_{r_i}^{r_o} \mu*(r)\left\{-n^3\left(\frac{R_n}{r}\right)^2 + n\left(\frac{\partial R_n}{\partial r}\right)^2\right\}\mathrm{d}r \times \int_{-\theta_c/2}^{\theta_c/2} \sin^2 n\theta\,\mathrm{d}\,\theta\right], \tag{B.7}$$

$$b_2 = -2n \times k_c\left(\frac{h}{2}\right)\int_{r_i}^{r_o} \mu*(r)R_n^2(r)\,\mathrm{d}r \times \int_{-\theta_c/2}^{\theta_c/2} \cos^2 n\theta\,\mathrm{d}\,\theta$$
$$- 2p_o \times n^3\left(\frac{h}{2}\right)^2\left[\int_{r_i}^{r_o} \mu*(r)\left(\frac{R_n}{r}\right)^2 dr \times \int_{-\theta_c/2}^{\theta_c/2} \sin^2 n\theta\,\mathrm{d}\,\theta\right]$$
$$+ 2p_o \times \left(\frac{h}{2}\right)^2\left[\int_{r_i}^{r_o} \mu*(r)\left\{n^3\left(\frac{R_n}{r}\right)^2 - n\left(\frac{\partial R_n}{\partial r}\right)^2\right\}\mathrm{d}r \times \int_{-\theta_c/2}^{\theta_c/2} \cos^2 n\theta\,\mathrm{d}\,\theta\right], \tag{B.8}$$

where $\mu* = \mu|_{\mathbf{f}=0}$ and $v_{,t} \equiv -h/2r \times \partial^2 w/\partial t\partial\theta$ and where $\mathbf{f}$ is the vector of system variables of μ. In automotive applications, $k_c \gg p_o(h/r^2)$ resulting in $b_1 > 0$ and $b_2 < 0$. Also, the modal damping coefficients are obtained from

$$D_1 = R_{d1} + N_{s1} + 2\xi_n\omega_n \quad \text{and} \quad D_2 = R_{d2} + N_{s2} + 2\xi_n\omega_n. \tag{B.9}$$

References

[1] N.M. Kinkaid, O.M. O'Reilly, P. Papadopoulos, Automotive disc brake squeal, *Journal of Sound and Vibration* 267 (2003) 5–166.
[2] H. Ouyang, W. Nack, Y. Yuan, F. Chen, Numerical analysis of automotive disc brake squeal: a review, *International Journal of Vehicle Noise and Vibration* 1 (2005) 207–231.
[3] H. Ouyang, J.E. Mottershead, M.P. Cartmell, M.I. Friswell, Friction-induced parametric resonances in discs: effect of a negative friction–velocity relationship, *Journal of Sound and Vibration* 209 (2) (1998) 251–264.
[4] H. Ouyang, J.E. Mottershead, D.J. Brookfield, S. James, M.P. Cartmell, A methodology for the determination of dynamic instabilities in a car disc brake, *International Journal of Vehicle Design* 23 (3-4) (2000) 241–262.
[5] H. Ouyang, J.E. Mottershead, W. Li, A moving-load model for disc–brake stability analysis, *ASME Journal of Vibration and Acoustics* 125 (1) (2003) 1–6.
[6] W.V. Nack, A.M. Joshi, Friction induced vibration: brake moan, Technical Report, 951095, *SAE Transactions*, Warrendale, PA, 1995.
[7] J. Flint, J. Hulten, Lining-deformation-induced modal coupling as squeal generator in a distributed parameter disc brake model, *Journal of Sound and Vibration* 254 (2002) 1–21.
[8] J.Y. Kang, C.M. Krousgrill, F. Sadeghi, Dynamic instability of a thin circular plate with friction interface and its application to disc brake squeal, *Journal of Sound and Vibration* 316 (2008) 164–179.
[9] J.Y. Kang, C.M. Krousgrill, F. Sadeghi, Analytical formulation of mode-coupling instability in disc–pad coupled system, *International Journal of Mechanical Science* 51 (2009) 52–63.
[10] J.Y. Kang, C.M. Krousgrill, F. Sadeghi, Comprehensive stability analysis of disc brake vibrations including gyroscopic, negative friction slope and mode-coupling mechanisms, *Journal of Sound and Vibration*, doi:10.1016/j.jsv.2009.01.050, in press.
[11] Y. Hu, L.I. Nagy, Brake squeal analysis using nonlinear transient finite element method, Technical Report, 971510, *SAE Transactions*, Warrendale, PA, 1997.
[12] D. Hochlenert, G.S. Korspeter, P. Hagedorn, Friction induced vibrations in moving continua and their application to brake squeal, *Journal of Applied Mechanics* 74 (2007) 542–549.
[13] J.D. Fieldhouse, T.P. Newcomb, Double pulsed holography used to investigate noisy brakes, *Optics and Lasers in Engineering* 25 (1996) 455–494.
[14] C. Talbot, J.D. Fieldhouse, Fourier analysis of holographic data from a noisy disc brake and its implication for modeling, *Proceedings of the Institution of Mechanical Engineers, Part D* 217 (2003) 975–984.
[15] M. Reeves, N. Taylor, C. Edwards, D. Williams, C.H. Buckberry, A study of brake disc modal behavior during squeal generation using high-speed electronic speckle pattern interferometry and near-field sound pressure measurements, *Proceedings of the Institution of Mechanical Engineers, Part D* 214 (2000) 285–296.
[16] R. Krupka, T. Walz, A. Ettemeyer, Fast and full-field measurement of brake squeal using pulsed ESPI technique, *Optical Engineering* 42 (5) (2003) 1354–1358.
[17] O. Giannini, F. Massi, Characterization of the high-frequency squeal on a laboratory brake setup, *Journal of Sound and Vibration* 310 (2008) 394–408.
[18] H. Lamb, R.V. Southwell, The vibrations of a spinning disc, *Proceedings of the Royal Society A* 99 (1921) 272–280.
[19] J.E. Mottershead, Vibration and friction induced instability in discs, *The Shock and Vibration Digest* 30 (1998) 14–31.
[20] M.T. Bengisu, A. Akay, Stability of friction-induced vibrations in multi-degree-of-freedom system, *Journal of Sound and Vibration* 171 (4) (1994) 557–570.
[21] R.I. Leine, D.H. Van Campen, A. De Kraker, L. Van Den Steen, Stick–slip vibrations induced by alternate friction models, *Nonlinear Dynamics* 16 (1998) 41–54.
[22] M.A. Heckl, Curve squeal of train wheels: unstable modes and limit cycles, *Proceedings of the Royal Society A* 458 (2002) 1949–1965.
[23] M. Denny, Stick–slip motion: an important example of self-excited oscillation, *European Journal of Physics* 25 (2004) 311–322.
[24] J.Y. Kang, S. Choi, Brake dynamometer model predicting brake torque variation due to disc thickness variation, *Journal of Automobile Engineering* 221 (2007) 49–55.